Zero : Jurnal Sains, Matematika, dan Terapan
E-ISSN : 2580-5754; P-ISSN : 2580-569X
Volume 10, Number 2, 2026
DOI: 10.30829/zero.v10i2.30793
Page: 841-857



Geoelectrical Delineation of Inactive Fault Paths for Foundation Design at IKN Sepaku

[1]Maraden Panjaitan
Master's Program in Civil Engineering, University of 17 August 1945 Samarinda, Indonesia

[2]Andi Sitti Astati
Department of Urban and Regional Planning, University of 17 August 1945 Samarinda, Indonesia

Article Info

Article history:

Accepted: 10 October 2026

Keywords:

Deep Foundation;
Displacement;
Fault Path;
Geoelectrical;
Geomembrane

ABSTRACT

This study delineated inactive fault paths in the Sepaku tourism area of Indonesia's new capital city, East Kalimantan, and translated the subsurface evidence into geotechnical design parameters. Two-dimensional geoelectrical resistivity surveys were conducted along two traverses of approximately 1,197 and 1,105 m, validated against outcrop and borehole observations, and converted into design values by reproducible closed-form methods. Resistivity ranged from 1.1 to 81.3 Ω·m, distinguishing weathered zones, bedding, and a fault zone of several discrete traces. Flexible pavement under a 400 kN reference load settled 9.5 mm, below the 20 mm serviceability threshold. A bored pile 0.8 m in diameter and 20 m deep gave an allowable capacity of 2,589 kN. An engineering buffer of 52.4 m was derived by summing the half-width of the fault-trace resistivity anomaly, a resolution allowance, and the extent of the imposed stress field. These values were site-specific and required validation before wider application.

This is an open access article under the CC BY-SA license.

Corresponding Author

Maraden Panjaitan,
Master's Program in Civil Engineering,
University of 17 August 1945 Samarinda, East Kalimantan, Indonesia
Email: maraden@untagsmd.ac.id

1. INTRODUCTION

Development of the Nusantara Capital City (IKN) in East Kalimantan has driven large-scale infrastructure construction, including tourism facilities in the Sepaku area. Such development requires a thorough understanding of subsurface geological conditions, particularly the presence of fault structures that may compromise foundation stability [1], [2]. In this study, an inactive fault is defined as a fault structure showing no evidence of surface rupture or seismic activity within the Holocene period, approximately the last 11,700 years. It is distinguished from an active fault, which exhibits historical or instrumentally recorded movement [3]. This distinction is established at the outset because much of the vulnerability literature discussed below concerns active faults, whereas the present study addresses residual geotechnical influence rather than seismic hazard from a structurally dormant fault.

Disaster vulnerability in fault zones is high because fault displacement can trigger earthquakes and secondary hazards such as liquefaction and landslides, amplifying the risk of damage to buildings and critical infrastructure [3], [4]. The regional tectonic setting and the distribution of major faults across Indonesia, which provide the broader seismic context for the study area, are presented in Figure 1.

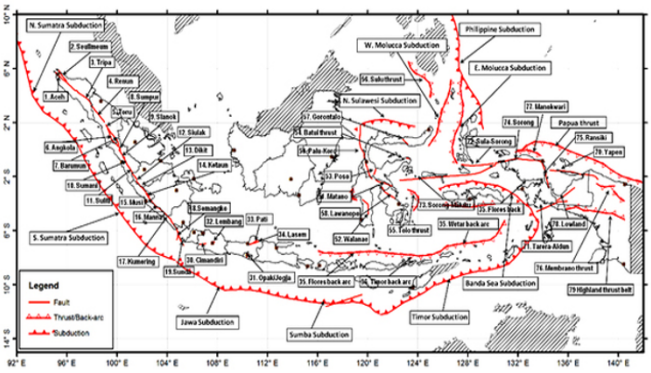


Figure 1. Tectonic and Fault Maps of Indonesia

Vulnerability is closely related to distance from a fault. Areas within roughly 1 km of an active fault experience the highest shaking intensity, while regions several kilometres away still face significant though reduced risk [5]. Local site conditions modify these effects further. Soft soils amplify seismic shaking even at moderate distances [5], and areas containing non-earthquake-resistant buildings or critical facilities such as gas pipelines and industrial installations are particularly exposed [6], [7]. Liquefaction potential is especially significant in medium-dense sandy soils near fault zones [4], [8]. Effective mitigation therefore depends on earthquake-resistant construction, hazard mapping, and spatial zoning supported by current geological and geophysical data [9].

Although the Sepaku faults are classified as inactive, their presence still influences subsurface rock strength, deformation patterns, and groundwater behaviour, all of which affect the safe design of pavements, deep foundations, retention ponds, and slopes [7], [10]. The distribution of these fault paths across the studied tourism area is shown in Figure 2. Among available subsurface investigation techniques, the geoelectrical resistivity method offers a non-destructive and cost-effective means of mapping subsurface layering, geological structures, and water-saturated zones, which suits the delineation of fault paths prior to construction [11], [12]. Technical guidelines for infrastructure crossing inactive fault zones, particularly for pavement thickness and foundation buffers, remain limited in current standards [13].

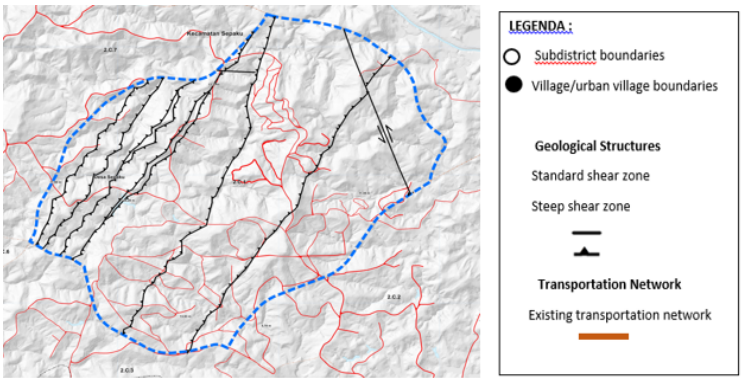


Figure 2. Fault Paths in the Tourism Area

Electrical resistivity imaging has been applied widely to the characterisation of fault structures, though with objectives that differ from those pursued here. Nabi et al. [14] applied electrical resistivity imaging to active faults for palaeoseismological reconstruction in Pakistan, focusing on rupture history rather than residual geotechnical properties. Faseki et al. [15] and Saad et al. [16] combined resistivity methods with cone penetration testing and geotechnical zoning respectively, but for general foundation characterisation and infrastructure safety zoning rather than fault-specific buffer design. Wei et al. [17] developed setback-distance theory explicitly for active fault contexts, where the governing concern is surface rupture hazard. Rizzo et al. [18] combined electrical resistivity and seismic reflection to unravel urban subsurface geology at a regional scale, illustrating the broader applicability of integrated geophysical characterisation to infrastructure planning. None of these studies translates the residual influence of an inactive fault on rock strength, deformation, and groundwater behaviour into quantitative pavement, pile, pond, and slope design parameters. That translation is the gap addressed here.

This study therefore aimed to identify inactive fault paths in the IKN Sepaku tourism area using two-dimensional geoelectrical surveys validated by field and borehole data, and to evaluate their implications for the design of road pavements, deep foundations, retention ponds, and slopes in order to recommend safer engineering design parameters. Specifically, it derives an engineering buffer for infrastructure adjacent to an

inactive fault trace from the measured lateral extent of the associated resistivity anomaly together with the extent of the stress field imposed by the foundation, and reports the pile capacity, pavement settlement, and slope gradients that follow for the site. Every design quantity is obtained by closed-form methods from parameters tabulated in this article, so that each can be reproduced independently. The contribution lies not in the geoelectrical method itself but in its translation into site-specific engineering buffers and design recommendations for inactive fault crossings, presented as a case study rather than a methodological advance.

2. RESEARCH METHOD

2.1 Research Design

This study combined two-dimensional (2D) geoelectrical resistivity surveys with field geological observation and closed-form geotechnical analysis in a quantitative geophysical and geotechnical approach. Resistivity contrasts distinguish subsurface materials and structural discontinuities such as faults effectively, while analytical geotechnical methods permit evaluation of their implications for infrastructure design from parameters that can be reported in full [11], [19].

2.2 Data Source and Variables

The primary data consisted of apparent resistivity values and topographic data collected along two survey traverses in the Sepaku tourism area, IKN, East Kalimantan, during the 2024 field campaign. These were supplemented by Dutch Cone Penetration Test (CPT/sondir) and Standard Penetration Test (SPT) data from a representative borehole. Secondary data comprised regional geological information and rock outcrop observations used for validation [20]. The principal observed variables were resistivity (ρ, in Ω·m), rock strength expressed as Rock Mass Rating, settlement under load, and slope geometry.

Geotechnical data available to this study comprise the logs of borehole BHC1-01 only. Further boreholes drilled within the wider consortium investigation are marked on the engineering geology sections but their logs were not available, as noted in §3.7.4.

Resistivity represents the ability of soil or rock to resist electrical current flow and varies systematically with material type. Water-saturated clay exhibits very low values of 1–30 Ω·m, water-saturated sand and gravel range from 30 to 200 Ω·m, volcanic rock from 200 to 1,000 Ω·m, and hard dry rock exceeds 1,000 Ω·m [11], [12].

2.3 Data Collection Procedure

The geoelectrical method injects electric current into the ground through a pair of current electrodes (A–B), while the resulting potential difference is recorded by a pair of potential electrodes (M–N). The measured voltage (V) and current (I) are converted into apparent resistivity (ρ_a) by applying a geometric factor (K) corresponding to the electrode configuration [9], [12].

A geoelectrical traverse is a line on the Earth's surface along which electrodes are placed and resistivity data are collected. Traverse layout was designed to capture subsurface geometry matching the target, to produce 2D cross-sections, and to avoid surface disturbances such as buildings, power lines, water pipes, and iron fences. Traverse direction was oriented perpendicular to the expected geological structure, and traverse length was determined by target depth following the practical rule that investigation depth is approximately 20% to 40% of traverse length. Survey lines were placed in open areas free of large metal objects, away from 220/380 V power sources, and with minimal traffic [9], [11]. This approach follows recommended engineering site investigation practice for foundation design in soils derived from shale and sandstone, where accurate delineation of weathered zones is critical for reliable subsurface characterisation [21].

Two-dimensional measurements were carried out using an AK Electronics Resistivity Instrument equipped with a 48-channel switch box in a roll-along Wenner–Schlumberger configuration, shown in Figure 4. Two traverses were surveyed. Traverse 1 (survey line 2C1-2), oriented northwest to southeast, spanned approximately 1,197 m between UTM coordinates (Zone 50S) 471,252.18 E / 9,902,658.86 N and 472,181.47 E / 9,901,903.35 N, coincident at its origin with borehole BHC1-01, and comprised 45 measurement configurations at 12.00 m electrode spacing giving 2,688 m of cumulative roll-along coverage. Traverse 2 (survey line 2C1-1), oriented west-northwest to east-southeast, spanned approximately 1,105 m between UTM coordinates 471,871.71 E / 9,902,155.19 N and 472,922.88 E / 9,901,814.39 N, and comprised 30 measurement configurations at 6.00 m electrode spacing giving 1,440 m of cumulative coverage. The origin of Traverse 2 lies on Traverse 1, approximately two thirds along its span. Several additional reference points were recorded along Traverse 1 without associated geotechnical borehole logs. A further short line of approximately 470 m was surveyed but excluded from the final research path because of accessibility constraints, and it is not analysed here. The site layout is shown in the survey location map (Figure 3).

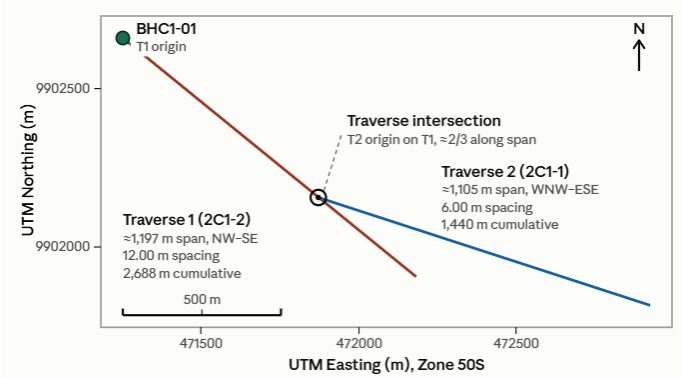


Figure 3. Site and traverse location map showing Traverse 1, Traverse 2, and borehole BHC1-01 (UTM Zone 50S). Traverse spans were computed from the reported endpoint coordinates; the figures of 2,688 m and 1,440 m denote cumulative roll-along coverage rather than ground distance. The origin of Traverse 2 lies on Traverse 1, approximately two thirds along its span. An additional line of approximately 470 m was surveyed but excluded from the final research path and is not shown.

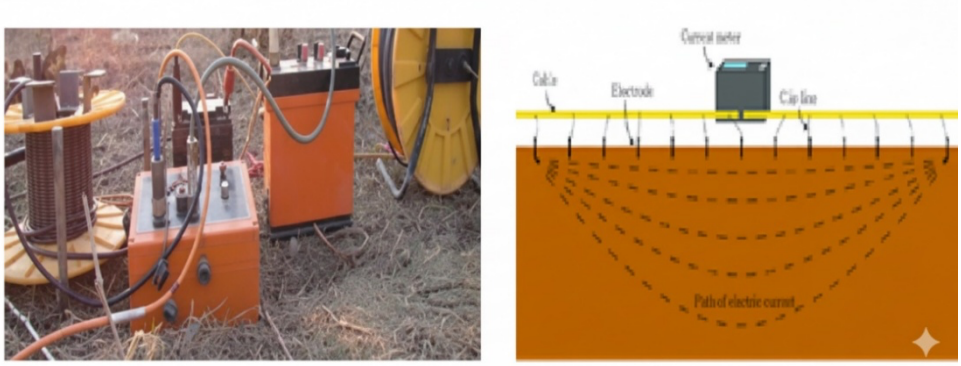


Figure 4. AK Electronics Resistivity Instrument with a 48channel switch box in a WennerSchlumberger configuration

Instrument calibration was performed through laboratory calibration and a pre-survey function check. Repeat measurements were taken at 5% of survey points to verify data reliability. These showed acceptable repeatability and support confidence in the field-recorded apparent resistivity values.

Data Availability Statement: The apparent resistivity dataset and the associated inversion model files were generated within the IKN research consortium and are subject to third-party access restrictions arising from the project's status. Derived data supporting the findings — including the parameters in Tables 1a, 1b and 2, the survey geometry in §2.3, and the analytical methods in §2.4 — are reported in full within this article and are sufficient to reproduce every design quantity presented. All geotechnical results reported in §3.3 and §3.4 were computed independently from these reported parameters.

2.4 Analytical Methods

Data processing and interpretation involved four stages. First, 2D inversion of the geoelectrical data was performed in Res2DInv over three iterations using a blocky (robust) constraint with a default damping factor of 0.1 to obtain true resistivity cross-sections. Inversion models are presented both without topographic correction (Figures 5 and 6) and with topographic correction applied (Figure 7), the latter forming the basis of the engineering geology interpretation in §3.2 and of the threshold-based measurements in §3.4.3. Elevation variation along the traverses is modest relative to the target investigation depth, and the two presentations do not differ materially in the position of the delineated structures. Second, subsurface geological conditions were determined by correlating resistivity data with regional secondary geological data and rock outcrops. Third, stratigraphic boundaries and geological structures were delineated using marker and zone systems. Fourth, resistivity horizon picks were generated to identify deposit boundaries and zones. Fault indications, expressed as discontinuous resistivity distributions or sudden low or high resistivity anomalies, were validated against surface data, borehole data, and the alignment of valleys and ridges [20], [22].

Geotechnical evaluation was conducted using closed-form analytical methods rather than numerical modelling, so that every reported design quantity can be reproduced from the parameters tabulated in this article without recourse to proprietary software or restricted model files.

Pavement settlement was computed by the Steinbrenner elastic method for a uniformly loaded flexible rectangular area on a semi-infinite elastic medium. The 400 kN reference load was represented as a distributed pressure of 25 kN/m² over a 2 m × 8 m footprint. Settlement at the centre of the loaded area was obtained by summing the corner contributions of four quadrants of 1 m × 4 m, using the corner influence factor for infinite depth given in Eq. (1a), with the subgrade parameters of Table 1a:

$$I = \frac{1}{\pi}\left[m \ln \frac{1+\sqrt{m^2+1}}{m} + \ln\left(m + \sqrt{m^2+1}\right)\right] \quad (1a)$$

$$s = \frac{q\, B'(1-\nu^2) I}{E} \quad (1b)$$

where m = L′/B′ for the quadrant, B′ and L′ are the quadrant dimensions, and q, ν and E are as defined above. The subgrade modulus of the 0–1 m interval was applied throughout the elastic half-space. Since the underlying units are substantially stiffer, reaching E = 55,000 kN/m² at the pile bearing depth (Table 1b), this treatment overstates compressibility and the computed settlement is therefore an upper bound with respect to layer stiffness.

The extent of the zone influenced by the fault path was determined directly from the inversion sections rather than from modelled strength contours. The influence zone was defined as the lateral extent over which resistivity departs from the local background by $|\Delta \log_{10} \rho| > 0.15$, corresponding to approximately one contour interval, with the threshold stated in advance of measurement. A resolution allowance of one half of the electrode spacing was added, since the boundary of a zone cannot be located more precisely than the sampling interval of the survey that delineates it.

The clearance required between the pile group and the fault path was obtained by the equivalent raft method [23], [24]. An equivalent raft of the pile group plan dimensions was placed at two thirds of the pile embedment, the load was spread at 1 horizontal to 4 vertical from that level to the pile toe, and the lateral extent of the 0.1q stress isobar beneath the resulting loaded area was read from Fadum influence charts [19].

The friction angle for the pile bearing layer was derived using the Terzaghi and Peck empirical correlation with SPT-N, given in Eq. (1c). Parameters for the pavement subgrade layer were obtained from laboratory testing of samples recovered from the 0–1 m interval of borehole BHC1-01, since Eq. (1c) is not applicable at the low N_{60} values characteristic of that layer.

$$\varphi' = 27.5 + 0.3N_{60} - 0.00054N_{60}^2 \quad (1c)$$

Table 1a. Soil Parameters — Pavement Subgrade Layer (Depth 0–1 m)

Parameter	Symbol	Value	Unit
Cohesion	c	33	kPa
Friction angle	φ′	22	°
Elastic modulus	E	9,400	kN/m²
Poisson's ratio	ν	0.30	–
Unit weight	γ	18.2	kN/m³

Note: Poisson's ratio was not measured and is adopted at 0.30, a standard value for stiff clay subgrade [19]. It enters only the elastic settlement computation in §3.3, where the result is insensitive to variation across the plausible range of 0.25–0.35

Table 1b. Soil Parameters — Pile Bearing Layer (Depth ≈20 m, N_{60} = 60, Sandy Clay)

Parameter	Symbol	Value	Unit
Cohesion	c	13	kPa
Friction angle	φ′	44	°
Elastic modulus	E	55,000	kN/m²
Unit weight	γ	21.2	kN/m³

Source: Laboratory testing and SPT-N correlation, borehole BHC1-01, field campaign 2024.

Note: The bored pile capacities in §3.4 are computed from N_{60} directly through Eq. (2) and (3) and are therefore independent of φ′ and E. Table 1b is retained for site characterisation and to support the stiffness contrast argument in §3.3. The friction angle derives from the empirical SPT-N correlation in Eq. (1c), which carries uncertainty that the tabulated value does not represent; it should be read as indicative rather than as a measured quantity.

The ultimate bearing capacity of bored piles was computed as the sum of end bearing capacity (Qb) and shaft friction capacity (Qs), following the O'Neill and Reese method [25], [26] and the Coyle and Castello method as presented in [23], based on SPT-N and CPT data, given in Eq. (2) and (3):

$$Qb = qp \times Ap, \text{ where } qp = 57.5\ N_{60} \quad (2)$$

$$Qs = fs \times As, \text{ where } fs = 2.0\ N_{60} \quad (3)$$

Here Ap is the pile base cross-sectional area and As is the shaft surface area over the embedded pile length. The resulting ultimate capacity (Qu = Qb + Qs) was divided by a safety factor of 3. This applied value is more conservative than the minimum factor of safety of 1.5 required by SNI 8460:2017; the two are not additive. Recent studies have demonstrated the reliability of direct CPT- and SPT-based statistical methods for predicting bored pile bearing capacity [27], and have shown the importance of adequate site investigation for reliable pile resistance prediction in weathered shale formations, given the inherent geomaterial uncertainty of such intermediate geomaterials [28]. This is consistent with the shale and mudstone units identified here (Table 2). Comparative studies of SPT- and CPT-based methods inform the estimation of bored pile capacity in layered soils further [29].

2.5 Software and Tools

Geoelectrical inversion was carried out in Res2DInv, while stratigraphic boundaries and three-dimensional subsurface visualisation were processed in RockWorks and Surfer. Geotechnical evaluation was performed analytically using the closed-form methods set out in §2.4, computed in spreadsheet form; no proprietary geotechnical modelling software was used in the analyses reported here. The change of analytical basis from numerical to closed-form methods, and the corresponding revision of the Data Availability Statement, were agreed by all authors. Pavement and foundation design referred to SNI MDP 2017, MDP 2024, SNI 8460:2017, and the latest pavement manuals issued by the Indonesian Ministry of Public Works and Housing [6], [13], [30].

2.6 Ethical Considerations

This study did not involve human or animal subjects. Field data collection was conducted on infrastructure development land within the IKN Sepaku planning area under standard site-access procedures and did not require formal ethical clearance.

3. RESULT AND ANALYSIS

3.1 Geoelectrical Inversion Results

Two geoelectrical traverses were surveyed in the Sepaku tourism area during the 2024 field campaign. Traverse 1 (line 2C1-2), oriented northwest to southeast, spanned approximately 1,197 m and comprised 45 measurement configurations at 12.00 m electrode spacing giving 2,688 m of cumulative coverage, achieving an RMS data-misfit of 9.3% after three iterations under a blocky (robust) inversion constraint. Traverse 2 (line 2C1-1), oriented west-northwest to east-southeast, spanned approximately 1,105 m and comprised 30 measurement configurations at 6.00 m electrode spacing giving 1,440 m of cumulative coverage, achieving an absolute (L1) data-misfit of 3.1% under the same constraint.

Apparent resistivity across both traverses ranged from 1.1 to 81.3 Ω·m. Model resistivity recovered by inversion spans a wider range, extending to approximately 333 Ω·m in the topographically corrected section of Figure 7. All threshold-based measurements reported in this section and in §3.4.3 are made on model resistivity, and the colour scale of the panel being read is used in each case. These misfit values fall within a generally acceptable range for field resistivity data of this type, but they are reported explicitly to support a cautious reading of model reliability. A moderate data-misfit does not by itself confirm a unique or fully correct subsurface model. The delineated structure should therefore be interpreted alongside the independent borehole and outcrop validation presented in §3.2, which constrains the plausible model space. The inversion results are presented in Figure 5 for Traverse 1 and Figure 6 for Traverse 2.

Traverse 1, running relatively parallel to rock layering, displayed irregular high resistivity at shallow depths below 20 m, indicating topsoil and weathered rock, and regular low resistivity at depths greater than 20 m aligned with the rock dip direction [11], [12].

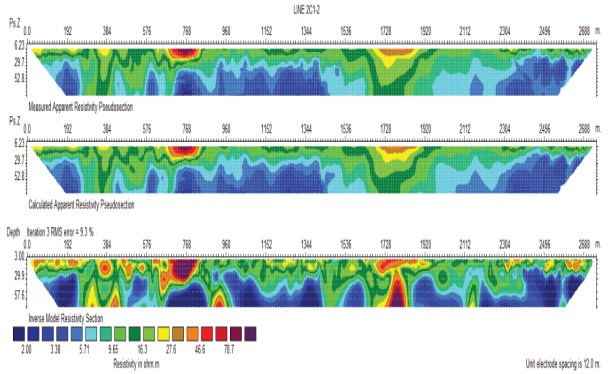


Figure 5. Inversion Results Without Topography, Traverse 1 (Survey Line 2C1-2)

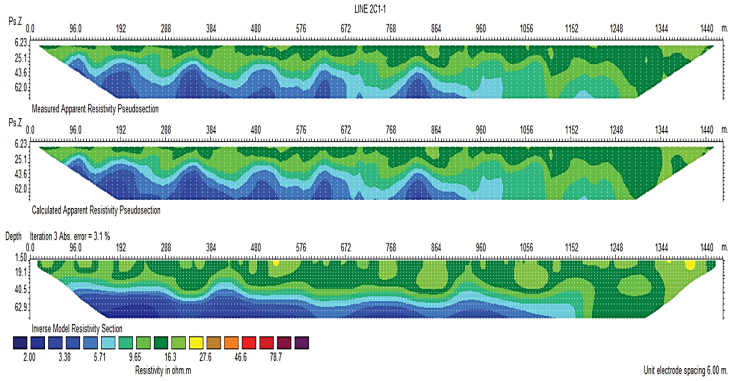


Figure 6. Inversion Results Without Topography, Traverse 2 (Survey Line 2C1-1)

The survey geometry permits an internal consistency check independent of the borehole and outcrop validation presented in §3.2. The origin of Traverse 2 lies on Traverse 1 at two thirds of its span, corresponding to chainage 1,792 m on the horizontal axis of Figure 7, computed from the reported endpoint coordinates on the assumption of a linear mapping between that axis and ground distance. Resistivity values were read from both inversion models at this common point at 5 m depth increments from 5 to 35 m, giving seven paired values. The lower bound of the window is set by the extent of model coverage at the terminus of Traverse 2, where the standard inversion no-data region begins at approximately 35 to 40 m depth, rather than by the depth of investigation of the array. The interval was set at 5 m rather than finer, this being the scale at which values can be read reliably from the sections. Agreement was assessed as $|\Delta \log_{10} \rho|$, resistivity being log-distributed, against a threshold of 0.15 adopted in advance and corresponding to approximately one contour interval.

The comparison returned a median $|\Delta \log_{10} \rho|$ of 0.57, and none of the seven paired values fell within the threshold. The divergence is systematic rather than scattered: recovered resistivity on Traverse 1 rises with depth from approximately 31 to 170 Ω·m across the window, while on Traverse 2 it falls from approximately 16 to 9 Ω·m. The two models therefore disagree in both magnitude and trend at the common point, and this is reported here rather than set aside.

Three features of the comparison bear on its interpretation. The common point lies adjacent to the most pronounced anomaly along Traverse 1, coincident with a mapped fault trace, in a zone of steep lateral gradient where a small horizontal error in the reading position translates into a large difference in recovered resistivity. On Traverse 2 the same point lies at the terminus of the line, where data density is lowest and edge effects in the inversion are largest. The two lines also differ in electrode spacing, 12.00 m against 6.00 m, so that Traverse 2 reaches a shallower depth of investigation and does not recover the deeper structure resolved by Traverse 1 within the window compared.

The check therefore does not corroborate the recovered resistivity magnitudes at the intersection, and the values reported from either model should be read with that in mind. It does not, however, bear on the delineated geometry, which is the quantity the analysis uses. The fault structure interpreted in §3.2 is present in both models at comparable position, and the threshold applied in §3.4.3 is referenced to the local background of the section being read rather than to absolute resistivity, so that the derived width is unaffected by a systematic offset between the two models. This is the only such comparison the survey geometry affords, the two traverses intersecting at a single point.

3.2 Geological Structure and Fault Identification

Geological structure analysis based on resistivity was indicated by discontinuous distributions and weak zones marked by sudden changes in resistivity values, subsequently validated using surface, borehole, and morphological data [20], [22], [31], [32]. As shown in the engineering geology cross-section (Figure 7), the subsurface was dominated by fair rock strength, but a fault zone comprising several discrete traces caused localised rock deformation and reduced rock mass quality at multiple points along the traverse. RMR values range from poor to fair, at RMR 35–58 and RQD 3–73%, across the stratigraphic sequence of mudstone, interlaminated sandstone and mudstone, silty mudstone, and shale units observed between 3 and 60 m depth in the borehole logs (Table 2). The regional survey context, within which Traverse 1 and Traverse 2 are highlighted, is shown in the resistivity fence diagram (Figure 8), which clarifies the spatial continuity of the weak zones relative to the broader survey grid.

Table 2. Rock Mass Classification by Depth Interval

Depth (m)	Material	SPT-N	RQD (%)	RMR	GSI
3–8	Mudstone	>60	33	46	22
8–10	Interlaminated sandstone & mudstone	>60	73	58	37
10–15	Mudstone	>60	39	50	27
15–19	Shale	>60	3	35	15
19–30	Mudstone	>60	31	43	20
30–37	Silty mudstone	—	68	55	30
37–40	Mudstone	—	18	41	15
40–42	Shale	—	13	36	15
42–47	Mudstone	—	27	40	17
47–60	Mudstone	—	69	55	29

Source: Borehole logging and rock mass classification, field campaign 2024.

Field observations of outcrops and boreholes identified fault indicators including slickenlines, mineral-filled fractures, and breccia zones, corroborated by resistivity anomalies around the fault traces. Discrimination between thrust and strike-slip mechanisms rests on field morphological evidence rather than on the resistivity sections, which resolve zone geometry but not slip sense. Ridge slope angles exceeding 60° with breccia zones containing rockslide material indicate thrust faults, while lateral displacements on ridges and river bends along the Sepaku River indicate strike-slip faults. This interpretation follows structural geology principles [1], [2]. The resulting fault paths and their associated landslide susceptibility zones are mapped in Figure 9.

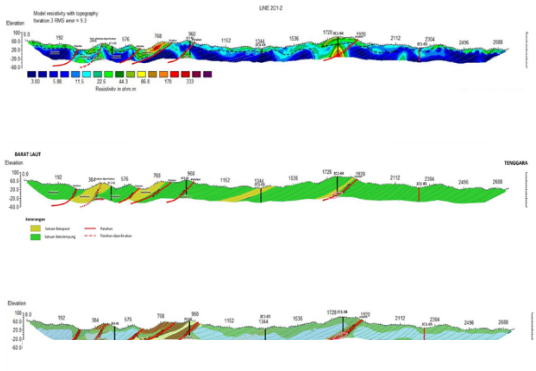


Figure 7. Engineering Geology Cross-Section of the Tourism Area (Traverse 1, Line 2C1-2)

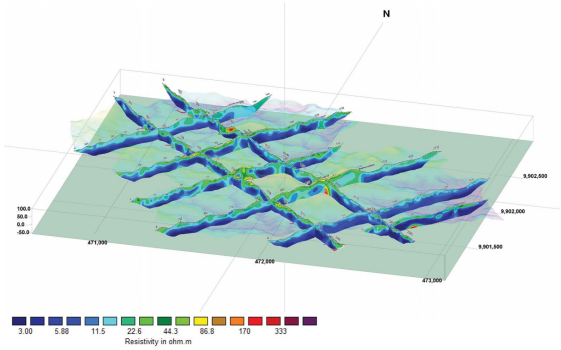


Figure 8. Regional Resistivity Fence Diagram, IKN Sepaku Survey Grid, with Traverse 1 and Traverse 2 Highlighted

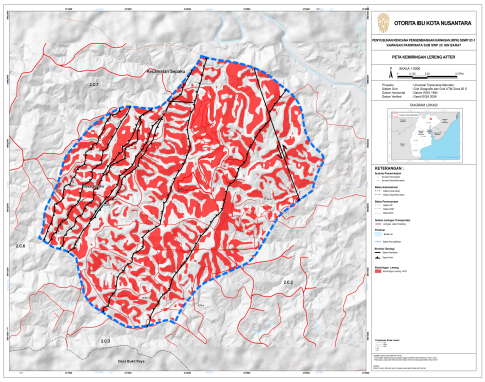


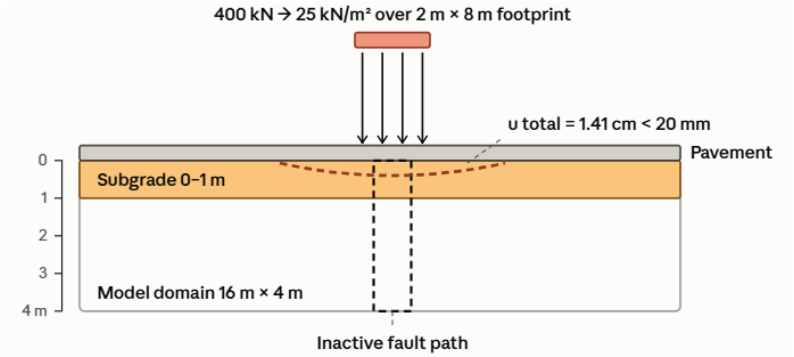
Figure 9. Fault Paths and Landslide Susceptibility Zones in the Tourism Area

3.3 Road Pavement on Fault Crossings

Explicit guidelines for pavement thickness at fault crossings remain limited within current standard specifications [13]. Settlement under the 400 kN reference load, applied as a distributed pressure of 25 kN/m² over a 2 m × 8 m footprint, was computed by the Steinbrenner elastic method using Eq. (1a) and (1b) with the pavement subgrade parameters of Table 1a. Summing the four quadrants of 1 m × 4 m, for which m = 4 and I = 0.982, gives a corner contribution of 2.38 mm and a centre settlement of 9.5 mm, well below the 20 mm serviceability threshold adopted in this study. The pavement cross-section on the fault path is shown in Figure 10.

The serviceability conclusion is insensitive to the method of computation. A numerical model of the same configuration, run within the consortium and reported at 14.1 mm, is consistent in order of magnitude with the analytical result and likewise falls below the threshold; the difference is of the sign expected, since the elastic solution does not represent plastic strain, while the analytical treatment is conservative with respect to layer stiffness for the reason given in §2.4. That model cannot be independently verified here and the analytical value is therefore adopted as the reported result.

Rigid pavement was not evaluated and is identified as a direction for future work (see §4). In inactive fault crossing zones, pavement design must account for even minor soil movement to prevent deformation-induced damage. Pavement thickness for such crossings is determined from traffic load, subgrade strength, and local geotechnical conditions following SNI MDP 2017 and MDP 2024, and these provisions indicate additional base-course thickness and a stronger surface layer for the conditions encountered here. Layer thicknesses were not the subject of the present analysis, which addressed settlement response under the reference load. Total settlement and flexural values, covering rutting and deflection, should remain below the same 20 mm threshold [13], [30].



Subgrade (Table 1a): $c \approx 33$ kPa, $\varphi' \approx 22°$, $E \approx 9{,}400$ kN/m², $\nu = 0.30$, $\gamma \approx 18.2$ kN/m³

Figure 10. Flexible pavement on the inactive fault crossing. The 400 kN reference load is applied as a distributed pressure of 25 kN/m² over a 2 m × 8 m footprint; using the subgrade parameters in Table 1a, the Steinbrenner elastic solution of Eq. (1a) and (1b) gives a centre settlement of 9.5 mm, below the 20 mm serviceability threshold adopted in this study. Settlement is exaggerated for legibility.

3.4 Deep Foundation

3.4.1 Bored Pile Capacity

The bored pile depth was set at 20.00 m with a diameter of 0.8 m. The foundation unit analysed here comprises 18 piles arranged in three rows of six at a spacing of three diameters, that is 2.40 m centre to centre, giving a plan of 5.60 m × 12.80 m measured to the outer pile faces. It was selected as the unit lying nearest the delineated fault path, and the analysis reports the resistance available from that configuration; the structural demand imposed on it lies outside the scope of this study and is not evaluated here.

Using the pile bearing layer parameters in Table 1b, with N_{60} = 60 in sandy clay, and Eq. (2) and (3), end bearing capacity was calculated as Qb = qp × Ap = 57.5 × 60 × 0.503 m² ≈ 1,734 kN, and shaft friction capacity as Qs = fs × As = 2.0 × 60 × 50.27 m² ≈ 6,032 kN, following the O'Neill and Reese [25], [26] and Coyle and Castello [23] approaches [29], [24]. Both unit values remain within the limits of the method, the base resistance of 3,450 kPa falling below the ceiling of 4,300 kPa and the unit shaft resistance of 120 kPa below the ceiling of approximately 200 kPa. Summing gives a total ultimate capacity of Qu ≈ 7,766 kN. Applying a safety factor of 3, above the minimum factor of safety of 1.5 required by SNI 8460:2017, yields an allowable bearing capacity of approximately Qallow ≈ 2,589 kN, based on SPT-N of 60 at 20 m depth and CPT data at the borehole location, using the dry drilling method. These quantities are computed from N_{60} directly and are independent of the friction angle and elastic modulus tabulated in Table 1b.

The direct SPT-based method was cross-checked against the total stress approach appropriate to cohesive material, since the bearing stratum is described as sandy clay. Taking $c_u \approx 6N_{60}$ gives 360 kPa, from which the base resistance $q_p = 9c_u$ is 3,240 kPa, within six per cent of the 3,450 kPa returned by Eq. (2). Unit shaft resistance by the α method, with α in the range 0.35 to 0.45 for a bored pile in very stiff clay, gives 126 to 162 kPa against the 120 kPa returned by Eq. (3), so that the adopted value is conservative in shaft resistance and closely convergent in base resistance. The direct method was retained as the primary basis, following the reliability of direct SPT- and CPT-based prediction reported for bored piles in comparable materials [27], [28].

Block failure was checked and does not govern. Taking $c_u \approx 6N_{60}$ = 360 kPa, the block capacity computed on a perimeter of 36.8 m over 20 m of embedment, together with base resistance of $9c_u$ over the block plan area of 71.7 m², exceeds the summed individual ultimate capacity of the 18 piles by a wide margin. A group efficiency of unity is therefore adopted, consistent with a spacing of three diameters in stiff cohesive material, and the allowable capacity per pile is applied without reduction.

3.4.2 Acceptance Criterion for the Engineering Buffer

The buffer separating the foundation from the fault path is required to satisfy a mutual condition: the pile group must lie beyond the zone within which the weakened path measurably influences ground response, and the stress field imposed by the pile group must not extend to that path.

The criterion adopted for the second leg is the conventional limit of significant stress influence, $\Delta\sigma \leq 0.1q$, which is the established basis for bounding the zone contributing to settlement in foundation analysis [19], [23]. Ground lying outside that isobar is by this convention not treated as contributing to the settlement of the loaded area, and the converse holds: a weakened band lying outside it does not contribute measurably to foundation settlement. For the configuration analysed here, the settlement increment corresponding to that stress level is below 1 mm, five per cent of the 20 mm serviceability threshold applied throughout this study. The criterion is therefore expressed in terms of stress extent, and is a standard rather than a bespoke one.

3.4.3 Leg One: Extent of Fault Influence

The delineated structure comprises several discrete fault traces distributed along the traverse rather than a single continuous zone (§3.2, Figure 7). The buffer is therefore derived for an individual trace, since each trace carries its own damage zone, and the width measured below is that of the resistivity anomaly associated with the trace nearest the proposed foundation. Where a foundation lies near more than one trace, the criterion applies to each independently.

The zone of fault influence was measured directly on the topographically corrected section of Figure 7 as the lateral extent over which resistivity departs from the local background by $|\Delta \log_{10}\rho| > 0.15$, the same threshold applied to the cross-traverse comparison in §3.1. A departure of 0.15 in $\log_{10}\rho$ corresponds to one interval of the colour scale of Figure 7, which spans 3.00 to 333 Ω·m at a ratio of 1.96 between labelled values, giving 0.146 in $\log_{10}$ per interval. The threshold and the reading unit therefore coincide, and the boundary of the anomaly was taken as the first colour interval departing from the local background.

Applying the threshold, the anomaly associated with the trace nearest the proposed foundation extends over 80.4 m, measured at the elevation of greatest lateral extent. The boundary was taken where the warm-toned response gives way to the intermediate-resistivity material that occurs continuously along the traverse and is not specific to the fault zone. The half-width measured from the centre of the zone is therefore 40.2 m. Values were digitised from the section at the scale printed, with a reading precision of the order of one contour cell. Where

the boundary could not be followed to a clear termination, the reading was taken at the last resolvable extent, so that the reported width is a lower bound on the zone.

A resolution allowance of one half of the electrode spacing was added. On Traverse 1, which carries the 12.00 m spacing, this allowance is 6.00 m. The allowance is not a discretionary margin: it follows from the resolution limit acknowledged in §3.7.2, since the boundary of the zone cannot be located more precisely than the interval at which the subsurface was sampled. Leg one therefore requires a clearance of 46.2 m from the centre of the delineated zone. The measured width of the damage zone associated with a single trace is an order of magnitude larger than the electrode spacing, so that the resolution allowance is small relative to the measured quantity. The allowance is retained for consistency of derivation but does not govern the resulting distance.

3.4.4 Leg Two: Extent of the Imposed Stress Field

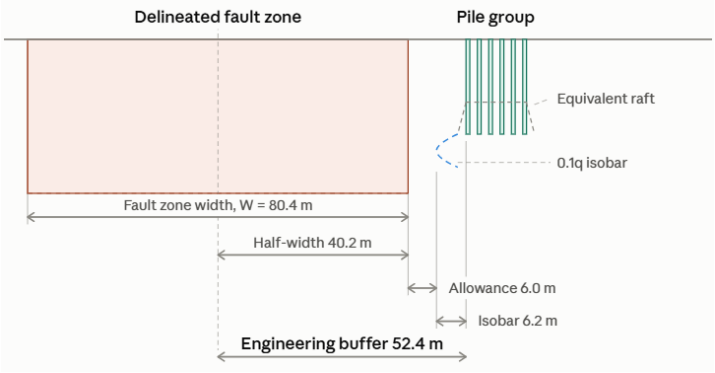
The lateral extent of the stress field imposed by the pile group was obtained by the equivalent raft method [23], [24]. An equivalent raft of the group plan dimensions, 5.60 m × 12.80 m, was placed at two thirds of the pile embedment, that is at 13.33 m below the pile cap. The load was spread at 1 horizontal to 4 vertical over the remaining 6.67 m to the pile toe, widening the loaded area by 1.67 m on each side to 8.94 m × 16.14 m at toe level.

The loaded area is rectangular with an aspect ratio of 1.81, so that the lateral extent of the 0.1q isobar differs between the two faces of the group. Since the orientation of the group relative to the delineated fault zone is not fixed by the present analysis, the controlling dimension was taken as the larger plan dimension of 16.14 m, giving a lateral extent beyond the loaded edge of 0.28 times that dimension, or 4.52 m [19]. Leg two therefore requires a clearance of 1.67 + 4.52 ≈ 6.2 m, measured from the outer face of the pile group. Adopting the smaller plan dimension instead would return 4.2 m, so the value carried forward is conservative with respect to group orientation and applies whichever face of the group lies nearest the fault zone. Repeating the computation for an alternative arrangement of two rows of nine at the same spacing returns a comparable value, the equivalent raft area changing little between arrangements of equal pile count, so the derived clearance is robust to the arrangement adopted.

3.4.5 Resulting Buffer

Summing the two legs gives a required separation of 46.2 + 6.2 = 52.4 m, measured from the centre of the delineated fault zone to the nearest pile face. The value is reported as computed and has not been rounded to a preferred figure. The buffer is referenced to the zone rather than to a single fault trace because the delineated structure comprises several discrete traces (§3.2) and the weakened ground between them forms part of the path to be excluded.

Both quantities entering this sum are reproducible from data reported in this article: the first from the inversion section against a stated resistivity threshold and the documented electrode spacing, the second from the pile group geometry and standard stress distribution charts. Neither depends on the interpretation of a strength contour, and neither requires access to model files. The buffer configuration is illustrated in Figure 11.



Bearing layer (Table 1b): c ≈ 13 kPa, φ′ ≈ 44°, E ≈ 55,000 kN/m², γ ≈ 21.2 kN/m³
Qb = 57.5 N_{60} × Ap, Qs = 2.0 N_{60} × As; dry drilling; SF = 3 > SNI 8460:2017 min. 1.5

Figure 11. Geometric definition of the engineering buffer. Leg one comprises the half-width of the resistivity anomaly delineated at $|\Delta \log_{10} \rho| > 0.15$, at 40.2 m from the centre of the zone, together with a resolution allowance of one half of the 12.00 m electrode spacing. Leg two comprises the lateral extent of the 0.1q stress isobar beneath an equivalent raft placed at two thirds of the pile embedment with a 1:4 spread to toe level, at 6.2 m from the outer pile face. The buffer, at 52.4 m, is the sum of the two legs, measured from the centre of the delineated fault zone to the nearest pile face. Horizontal and vertical scales are equal; pile diameter and the isobar boundary are exaggerated for legibility, and the isobar is indicated qualitatively.

3.5 Retention Pond Foundation

Geomembranes were applied to protect ponds (embung), polders, and fault-adjacent paths against water loss through seepage, erosion, or infiltration. These synthetic impermeable sheets, made of HDPE, PVC, or EPDM, and particularly Type 1 HDPE, exhibit elongation values of 300% to 700%, allowing them to stretch three to seven times their original length before rupture and thereby accommodate minor ground movement near fault zones [33], [34]. The retention pond foundation design is shown in Figure 12.

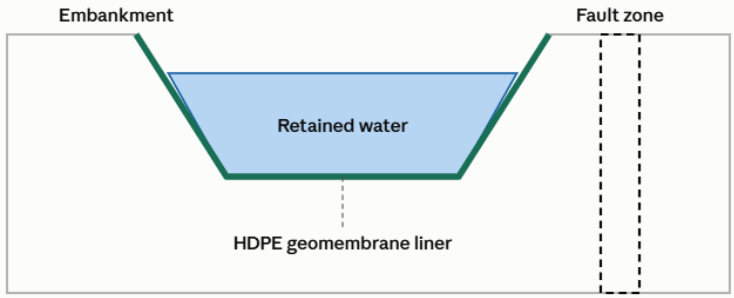


Figure 12. Retention pond foundation with geomembrane lining (design detail). A Type 1 HDPE geomembrane lines the side slopes and base, with elongation at break of 300–700%, three to seven times its original length, resisting water loss by seepage, erosion, and infiltration in the fault-adjacent zone. The specification derives from the material properties reported in [33] and [34]. Pond dimensions were not determined in this study; the figure is not to scale.

3.6 Slope Stability

Slopes and benches in clay shale containing montmorillonite developed residual shear strength when wet, which reduced stability drastically [35], [36], [37] . For shale and clay shale, slope inclinations were therefore required to be gentler than for pure clay, with a recommended minimum of 3H:1V to 4H:1V to prevent landslides. Where necessary, stability was enhanced using retaining walls or secant piles, validated through stable and unstable condition analyses [19]. The recommended slope geometry is presented in Figure 13.

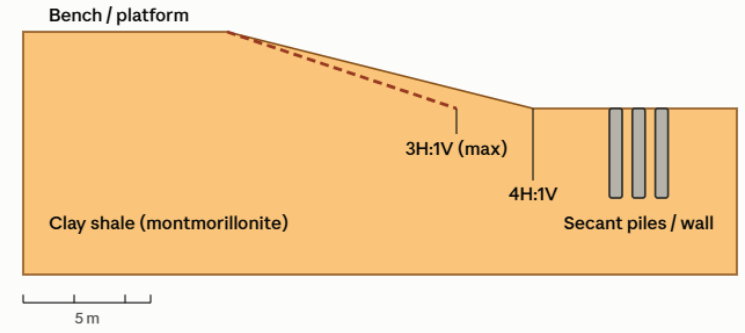


Figure 13. Recommended slope geometry in clay shale (design detail). The drawn slope surface corresponds to a 4H:1V gradient and the dashed line to the steepest recommended gradient of 3H:1V. Clay shale containing montmorillonite develops residual shear strength when wet, requiring gradients flatter than those adopted for pure clay; the recommended range derives from the residual-strength literature cited in [35], [36] and [37]. Secant piles or a retaining wall may be added near the toe where additional stability is required. The scale bar applies equally to the horizontal and vertical directions.

3.7 Discussion

3.7.1 Comparison with Existing Standards and Prior Studies

The buffer derived here is a summed clearance, comprising the extent of the delineated fault zone with its resolution allowance and the lateral extent of the imposed stress field, referenced to the centre of the zone. Published setback and safety-zoning distances are generally referenced to a fault trace and governed by a different criterion. Any comparison is therefore a comparison between quantities of different kinds unless the reference point and the governing criterion are matched, and the discussion below is qualified accordingly.

On that basis, the present buffer is larger than the general infrastructure safety-zoning distances reported by Saad et al. [16] for the Cairo ring road case. This difference is consistent with the closer proximity assumed here between tourism infrastructure and an identified fault zone, but it should not be read as a straightforward indication that the present recommendation is more conservative, since the two studies do not define their distances against the same reference and the safety-zoning distances in [16] address a different design question. A comparable limitation applies to the integrated geophysical approach of Rizzo et al. [18], which operates at a

regional characterisation scale and does not translate its results into site-specific foundation design parameters, so it offers no directly comparable buffer distance. The absence of such a comparator across the studies reviewed here is itself part of the gap this study addresses.

The buffer derived here, at 52.4 m, is substantially larger than the 20 m value reported in earlier consortium documentation for the same site. The difference arises from the reference point and the measured quantity rather than from any change of criterion. The present derivation measures the width of the resistivity anomaly associated with an individual fault trace, at 80.4 m, and references the buffer to the centre of that zone, whereas the earlier value was estimated as a margin beyond an idealised representation of the fault path without a documented threshold. The larger distance is a consequence of measuring the weakened zone rather than estimating a margin beyond an idealisation of it, and it indicates that the earlier figure understated the separation required.

The distinction from active-fault studies is more fundamental than one of magnitude. Unlike the palaeoseismological resistivity work of Nabi et al. [14], which characterises rupture history along active faults, the present buffer addresses residual geotechnical influence rather than seismic hazard, and it is therefore not directly comparable to active-fault setback distances [17] in either magnitude or purpose. The governing criterion also differs in structure. Active-fault setback is governed by rupture avoidance in one direction only, whereas the requirement satisfied here is mutual: the foundation is kept outside the zone of residual fault influence, and the loaded zone is kept clear of the weakened path. This bidirectional criterion gives the recommended distance its rationale, and it has no direct counterpart in the setback literature cited above.

Against existing standards, the position is one of absence rather than divergence. SNI 8460:2017 [6] establishes geotechnical design requirements including the minimum factor of safety applied to the pile capacities reported in §3.4, and SNI MDP 2017 [13] and MDP 2024 [30] govern pavement thickness determination, but none of these standards specifies a setback or buffer distance for infrastructure crossing an inactive fault zone. The buffer proposed here therefore supplements rather than contradicts the standards applied elsewhere in this study, and it should be treated as a site-specific derivation advanced in the absence of a normative provision rather than as an alternative to an existing requirement.

3.7.2 Non-Uniqueness and Resolution Limits

Two properties of the resistivity method bound what the delineated fault geometry can be taken to show, and both warrant explicit statement.

The first concerns non-uniqueness. As noted in §3.1, the data-misfits obtained for the two traverses, 9.3% RMS for Traverse 1 and 3.1% L1 for Traverse 2, fall within an acceptable range for field data of this type, but a low misfit does not establish that the recovered model is correct or that it is the only model consistent with the measurements. Different resistivity distributions can reproduce the same surface response. The fault zone inferred here, comprising several discrete traces rather than a single continuous surface, should therefore be read as the most plausible model consistent with the available borehole and outcrop constraints rather than as a uniquely resolved structure.

The second concerns resolution. Electrode spacings of 12.00 m on Traverse 1 and 6.00 m on Traverse 2 set the scale of the smallest features the surveys can distinguish. Neither survey can resolve structural detail below that scale, and the boundaries of the delineated zone should be understood as approximate to within approximately one half of the spacing, which is the allowance carried into the derivation in §3.4.3.

The cross-traverse consistency check described in §3.1 exploits the one point at which the two independent inversions overlap and provides a constraint on model uncertainty that is independent of the borehole and outcrop validation of §3.2. It returned a median departure of 0.57 in $\log_{10}\rho$, indicating that recovered resistivity magnitudes are not corroborated at that point, for the reasons of survey geometry set out there.

Two further lines of work would strengthen confidence in the delineated geometry: computation of a depth-of-investigation index to establish the depth beyond which the model is no longer constrained by the data, and comparison of smooth and robust inversions of the same dataset to assess how far the inferred structure depends on the regularisation chosen. Neither was undertaken here, since both require access to the raw inversion files, which are subject to the restrictions stated in the Data Availability Statement.

3.7.3 Transferability of Active-Fault Setback Theory

Setback distance theory [17] was developed primarily for active fault contexts, where the governing hazard is surface rupture. Applying an analogous buffer concept to an inactive fault, as done here, shifts the design basis from rupture avoidance to residual influence control. The 52.4 m buffer derived in this study is therefore not transferable to active fault settings without re-evaluation against seismic rupture hazard criteria. Conversely, active-fault setback distances from the literature should not be applied uncritically to inactive fault infrastructure planning.

3.7.4 Practical Significance and Boundaries

The design recommendations are directly applicable to the Sepaku tourism area, but they are not all governed by the same conditions and their boundaries differ accordingly. The bored pile capacity, the pavement settlement, and the slope gradients apply under the loading and soil conditions considered, comprising borehole BHC1-01, the 400 kN reference load, and static conditions. The buffer is conditioned on the delineated extent of the fault zone and on the pile group geometry from which the stress field was derived, and the geomembrane specification rests on the elongation range of the material rather than on any loading case. None of these recommendations should be generalised to other inactive fault zones, different soil stratigraphy, or dynamic and seismic loading without independent validation.

The geotechnical characterisation rests on a single logged borehole, and the significance of this constraint warrants precise statement. The role of BHC1-01 in this study is calibration rather than spatial coverage: it establishes the correspondence between resistivity value and material type at one location, against which the inversion sections are interpreted. Spatial coverage is supplied by the inversion sections themselves, which extend over 1,197 m and 1,105 m and resolve lateral continuity along both traverses. This division of evidence, in which a borehole anchors the interpretation and the geophysical section carries the lateral extension, is the normal basis of geophysical site characterisation, and the single borehole should be read against that role rather than as an attempt to represent the site by point sampling.

The engineering geology sections of Figure 7 carry positional markers for three further boreholes along Line 2C1-2, designated BC1-03, BC1-04 and BC1-05. These markers record the drilling programme of the wider consortium investigation and are retained in the figure as surveyed, but the corresponding logs were not available to this study. No stratigraphic, SPT or rock mass data from those locations enter the analysis reported here, and the characterisation rests on BHC1-01 alone. Their positions are noted because they identify where corroborating data would most directly test the spatial representativeness of the derived parameters, should the logs become available.

Three features of the analysis limit the exposure of the results to parameter uncertainty at that single point. The pile capacities are computed from N_{60} directly through Eq. (2) and (3) and are independent of the cohesion, friction angle and elastic modulus derived at the borehole. The buffer derivation depends on the pile group geometry and on the resistivity sections, not on the borehole parameters. Only the pavement settlement depends on a laboratory-derived stiffness, and the applied safety factor of 3, twice the minimum of 1.5 required by SNI 8460:2017, accommodates parameter variability well beyond the range plausible for a stratigraphy that returns N_{60} exceeding 60 continuously from 3 to 30 m depth (Table 2).

These considerations bound the constraint but do not remove it. Corroboration from additional boreholes away from the fault zone would allow the resistivity-to-material calibration to be tested at more than one location and would strengthen confidence in the spatial representativeness of the derived soil parameters. It is recommended for future site investigation phases.

4. CONCLUSION

This study demonstrated that a two-dimensional geoelectrical resistivity survey, validated by outcrop and borehole observations and translated directly into geotechnical design parameters, provides a workable methodology for infrastructure planning across inactive fault zones. Two elements of that work are generalisable. The first is the workflow itself, running from resistivity delineation, through validation against independent subsurface evidence, to the derivation of quantitative design parameters by closed-form methods that a reader can reproduce. The second is the principle governing the buffer: for an inactive fault, the distance should be referenced to the measured extent of the weakened zone rather than to an idealisation of the fault path, and it should satisfy a mutual criterion, keeping the foundation outside the zone of residual influence while keeping the imposed load clear of the weakened path. The numerical values reported below are outputs of that workflow at one site rather than transferable results.

At IKN Sepaku, the workflow produced the following outputs. The fault zone was delineated on the topographically corrected inversion section at a resistivity departure threshold of $|\Delta \log_{10} \rho| > 0.15$, returning a width of 80.4 m for the trace nearest the proposed foundation, and an engineering buffer of 52.4 m was derived from its half-width together with a resolution allowance of one half of the electrode spacing, summed with the lateral extent of the 0.1q stress isobar beneath an equivalent raft at two thirds of the pile embedment, measured from the centre of the delineated zone to the nearest pile face (§3.4). A bored pile 20 m deep and 0.8 m in diameter yielded an ultimate capacity of approximately 7,766 kN and an allowable capacity of approximately 2,589 kN at a safety factor of 3, above the minimum of 1.5 required by SNI 8460:2017, as computed from Eq. (2) and (3) with $N_{60} = 60$ (§3.4). Flexible pavement under the 400 kN reference load, applied as 25 kN/m² over a 2 m × 8 m footprint, produced a centre settlement of 9.5 mm by the Steinbrenner elastic method, below the 20 mm serviceability threshold adopted in this study (§3.3). Retention ponds were recommended to be lined

with Type 1 HDPE geomembrane (§3.5), and slope gradients of 3H:1V to 4H:1V were recommended for clay shale (§3.6). These values are specific to the surveyed traverses, which returned data-misfits of 9.3% RMS and 3.1% L1 (§3.1), to the representative borehole profile BHC1-01, and to the static loading case.

Five limitations bound these findings. The geotechnical characterisation rests on a single logged borehole under static loading, in the calibration role set out in §3.7.4; three further boreholes are marked along the traverse but their logs were not available to this study. The analysis is confined to closed-form elastic and limit-state methods, so that stress redistribution and plastic strain around the weakened path are not represented and the pavement settlement in particular should be read as an elastic estimate rather than a full deformation response. The foundation analysis reports resistance, not deformation: for a group of 18 piles the overlapping stress fields of the individual piles mobilise a settlement appreciably greater than that of a single pile, governed by the stiffness of the strata beneath toe level, which the available borehole data do not characterise; group settlement was therefore not evaluated and requires separate assessment before the configuration is adopted in design, particularly given the proximity of the weakened zone. Only flexible pavement was evaluated, leaving rigid pavement performance under equivalent fault-crossing conditions unassessed. Finally, the cross-traverse comparison at the intersection returned a median departure of 0.57 in $\log_{10}\rho$, indicating that recovered resistivity magnitudes at that location are not corroborated between the two independent inversions; the delineated geometry on which the design derivation rests is unaffected, but absolute resistivity values reported from either section carry corresponding uncertainty. A further constraint is external to the analysis: no published buffer distance for an inactive fault crossing was identified against which the derived value could be benchmarked, so the recommendation stands without an external point of comparison.

These limitations set the direction for further work. Priority lies with additional borehole investigation away from the fault crossing to test the spatial representativeness of the derived soil parameters, beginning with the three locations already marked along the traverse, and with group settlement analysis for the configuration reported here. Numerical verification of the analytical buffer derivation, once model files or modelling software become available, would allow the closed-form result to be checked against a full deformation analysis. Beyond these, the delineated geometry would be strengthened by inversion sensitivity analysis and by repeat resistivity surveys with lower data-misfit targets to assess temporal change in fault-zone conditions. Extension of the design analysis would require rigid pavement evaluation for comparison, dynamic seismic loading scenarios, and long-term displacement monitoring instrumentation installed at the recommended buffer zone.

5. REFERENCES

[1] M. P. Billings, *Structural Geology*, 4th ed. New Delhi: Prentice-Hall of India, 1972.

[2] P. de Genevraye and L. Samuel, "Geology of the Kendeng zone (Central and East Java)," in *Proceedings of the 1st Annual Convention of the Indonesian Petroleum Association*, Jakarta, 1972, pp. 17–30.

[3] Badan Standardisasi Nasional, "SNI 1726:2019 Tata Cara Perencanaan Ketahanan Gempa untuk Struktur Bangunan Gedung dan Non-Gedung," Jakarta, 2019.

[4] R. A. K. Mahli, S. P. Dewi, P. B. C. Manullang, H. W. Utama, and R. Mulyasari, "Identifikasi zona potensi likuifaksi di Kota Bandar Lampung berdasarkan analisis data spasial," *Jurnal Geofisika Eksplorasi*, vol. 10, no. 3, pp. 217–227, 2024, https://doi.org/10.23960/jge.v10i3.429.

[5] J. H. Lee, A. Ansari, H. An, and J. Y. Jeong, "Seismic loss and resilience modeling of bridges in soft soils: towards the design of sustainable transportation infrastructure facilities," *Sustain. Resilient Infrastruct.*, vol. 9, no. 5, pp. 473–495, 2024, https://doi.org/10.1080/23789689.2024.2328979.

[6] Badan Standardisasi Nasional, "SNI 8460:2017 Persyaratan Perancangan Geoteknik," Jakarta, 2017.

[7] H. C. Hardiyatmo, *Analisis dan Perencanaan Fondasi I*, 3rd ed. Yogyakarta: Gadjah Mada University Press, 2017.

[8] A. Zakariya, F. Nurdiansyah, C. T. S. A. Galag, and J. Situmorang, "Analisis kuantitatif dan kualitatif potensi likuefaksi di area tanah kepasiran medium-padat dekat Sesar Opak," *Jurnal Jalan-Jembatan*, vol. 39, no. 2, pp. 74–87, 2022.

[9] J. M. Reynolds, *An Introduction to Applied and Environmental Geophysics*, 2nd ed. Chichester: Wiley-Blackwell, 2011.

[10] H. C. Hardiyatmo, *Analisis dan Perencanaan Fondasi II*, 3rd ed. Yogyakarta: Gadjah Mada University Press, 2015.

[11] M. H. Loke and R. D. Barker, "Rapid least-squares inversion of apparent resistivity pseudosections by a quasi-Newton method," *Geophys. Prospect.*, vol. 44, no. 1, pp. 131–152, 1996, https://doi.org/10.1111/j.1365-2478.1996.tb00142.x.

[12] M. H. Loke, J. E. Chambers, D. F. Rucker, O. Kuras, and P. B. Wilkinson, "Recent developments in the direct-current geoelectrical imaging method," *J. Appl. Geophy.*, vol. 95, pp. 135–156, 2013, https://doi.org/10.1016/j.jappgeo.2013.02.017.

[13] Kementerian Pekerjaan Umum dan Perumahan Rakyat, "Manual Desain Perkerasan Jalan (MDP) 2017," Jakarta, 2017.

[14] A. Nabi, X. Liu, Z. Gong, and A. Ali, "Electrical resistivity imaging of active faults in palaeoseismology: case studies from Karachi Arc, southern Kirthar Fold Belt, Pakistan," *NRIAG Journal of Astronomy and Geophysics*, vol. 9, no. 1, pp. 116–128, 2020, https://doi.org/10.1080/20909977.2020.1722524.

[15] O. E. Faseki, A. O. Ademeso, K. I. Adebayo, O. Olasunkanmi, and T. B. Omoyajowo, "Foundation characterization in Ikate area southwestern Nigeria using electrical resistivity tomography and cone penetration test," *Engineering Heritage Journal*, vol. 6, no. 2, pp. 51–57, 2022, https://doi.org/10.26480/gwk.02.2022.51.57.

[16] A. M. Saad, M. A. H. Sakr, and M. S. A. Selim, "Geotechnical and geophysical investigations for infrastructure safety zones: a case study of the supporting ring road, Cairo, Egypt," *Sci. Rep.*, vol. 14, p. 29670, 2024, https://doi.org/10.1038/s41598-024-72337-8.

[17] L. Wei, X. Xu, and F. Li, "Theory and application of setback distance from active faults," *Coal Geology and Exploration*, vol. 51, no. 12, p. 15, 2023, https://doi.org/10.12363/issn.1001-1986.23.11.0768.

[18] E. Rizzo *et al.*, "Deep geophysical investigations (DERT and Seismic Reflection) to unravel the Ferrara urban area geology," *Geomatics, Natural Hazards and Risk*, vol. 15, no. 1, 2024, https://doi.org/10.1080/19475705.2024.2423748.

[19] J. E. Bowles, *Foundation Analysis and Design*, 5th ed. New York: McGraw-Hill, 1996.

[20] W. M. Telford, L. P. Geldart, and R. E. Sheriff, *Applied Geophysics*, 2nd ed. Cambridge: Cambridge University Press, 1990.

[21] F. O. Olusola, "Engineering site investigation for foundation design and construction in shale and sandstone derived soils of Okitipupa area, southwestern Nigeria," *Journal of Applied Geology*, vol. 6, no. 1, pp. 62–76, 2021, https://doi.org/10.22146/jag.55091.
[22] M. H. Loke, I. Acworth, and T. Dahlin, "A comparison of smooth and blocky inversion methods in 2D electrical imaging surveys," *Exploration Geophysics*, vol. 34, no. 3, pp. 182–187, 2003, https://doi.org/10.1071/EG03182.
[23] B. M. Das and N. Sivakugan, *Principles of Foundation Engineering*, 9th ed. Boston: Cengage Learning, 2018.
[24] M. Tomlinson and J. Woodward, *Pile Design and Construction Practice*, 6th ed. Boca Raton: CRC Press, 2014.
[25] M. W. O'Neill and L. C. Reese, "Drilled Shafts: Construction Procedures and LRFD Design Methods," Washington, DC, 1999.
[26] H. G. Poulos and E. H. Davis, *Pile Foundation Analysis and Design*. New York: John Wiley and Sons, 1980.
[27] H. Alielahi, D. Mousavi, and Z. Nadernia, "Statistical assessment of bearing capacity of cast-in-situ bored piles using direct CPT and SPT methods: A case study," *Indian Geotechnical Journal*, vol. 53, pp. 698–714, 2023, https://doi.org/10.1007/s40098-022-00690-4.
[28] O. E. Oluwatuyi, K. Ng, and S. S. Wulff, "Improved resistance prediction and reliability for bridge pile foundation in shales through optimal site investigation plans," *Reliab. Eng. Syst. Saf.*, vol. 239, p. 109476, 2023, https://doi.org/10.1016/j.ress.2023.109476.
[29] S. S. Abadi, R. Roestaman, and S. Permana, "Analisis perbandingan kapasitas kuat dukung pondasi bore pile berdasarkan hasil pengujian SPT dan CPT," *Jurnal Konstruksi*, vol. 19, no. 2, pp. 549–560, 2022, https://doi.org/10.33364/konstruksi/v.19-2.920.
[30] Kementerian Pekerjaan Umum dan Perumahan Rakyat, "Manual Desain Perkerasan Jalan (MDP) 2024," Jakarta, 2024.
[31] Q. Y. Zhou, H. Matsui, and J. Shimada, "Characterization of the unsaturated zone around a cavity in fractured rocks using electrical resistivity tomography," *Journal of Hydraulic Research*, vol. 42, no. sup1, pp. 25–31, 2004, https://doi.org/10.1080/00221680409500044.
[32] E. Rizzo and V. Giampaolo, "New deep electrical resistivity tomography in the High Agri Valley basin (Basilicata, Southern Italy)," *Geomatics, Natural Hazards and Risk*, vol. 10, no. 1, pp. 197–218, 2019, https://doi.org/10.1080/19475705.2018.1520150.
[33] R. M. Koerner, *Designing with Geosynthetics*, 6th ed. Bloomington: Xlibris, 2012.
[34] M. Z. Islam, B. A. Gross, and R. K. Rowe, "Degradation of exposed LLDPE and HDPE geomembranes: A review," in *GeoFrontiers 2011*, Dallas, TX, 2011, pp. 2065–2072. https://doi.org/10.1061/41165(397)211.
[35] N. R. Morgenstern and K. D. Eigenbrod, "Classification of argillaceous soils and rocks," *Journal of the Geotechnical Engineering Division, ASCE*, vol. 100, no. 10, pp. 1137–1156, 1974.
[36] L. D. Wesley, *Mechanics of Residual Soils*, 2nd ed. Boca Raton: CRC Press, 2010.
[37] G. Pamungkas, T. Putranto, S. Suharyanto, M. Muhrozi, and Y. Priambodo, "Residual strength parameter method for slope stability on a toll road with expansive clay," *Journal of Geoscience, Engineering, Environment and Technology*, vol. 7, no. 2, pp. 49–58, 2022, https://doi.org/10.25299/jgeet.2022.7.2.9251.